

Design, fabrication and testing of microlens arrays for sensors and microsystems

Ph Nussbaum†§, R Völkel†, H P Herzig†, M Eisner‡ and S Haselbeck‡

† Institut de Microtechnique Neuchâtel, Rue A-L Breguet 2, CH-2000 Neuchâtel, Switzerland

‡ University of Erlangen–Nürnberg, Applied Optics, Staudtstraße 7, D-95108 Erlangen, Germany

Abstract.

We report on our activities in design, fabrication, characterization and system integration of refractive microlens arrays for sensors and microsystems. Examples for chemical analysis systems (μ TAS, blood gas sensor), neural networks and multiple pupil imaging systems for photolithography (microlens and smart mask lithography) are presented.

1. Introduction

Microfabrication technologies such as photolithography and resist processing (reflow) were used to manufacture arrays of refractive microlenses in photoresist. The microlenses were transferred in fused silica by reactive ion etching (RIE) and replicated in polycarbonate and epoxy by embossing and casting techniques. The surface profile and the wave aberrations were characterized by interferometric testing. The surface roughness was measured by atomic force microscopy.

First we summarize the basic physical and optical properties of plano-convex refractive microlens arrays. We explain the fabrication and testing of microlens arrays. Examples for microsystems using lens arrays are presented.

2. Properties of plano-convex refractive microlens arrays

A plano-convex microlens is described by the lens diameter \emptyset , the height at the vertex h_L , the radius of curvature R , the refractive index n and the contact angle α as shown in figure 1(a). Figure 1(b) shows a scheme of a rectangular (left) and a hexagonal packed lens array (right).

2.1. Radius of curvature and focal length

The lens profile $h(r)$ of an axial symmetrical plano-convex lens is generally described by

$$h(r) = \frac{1}{R} \frac{r^2}{1 + \sqrt{1 - (K + 1)r^2/R^2}} + \text{higher-order terms} \quad (1)$$

where h is the height of the lens as a function of the distance r to the optical axis, R is the radius of curvature at the vertex and K is the aspherical constant. The lens profile

§ E-mail address: philippe.nussbaum@imt.unine.ch

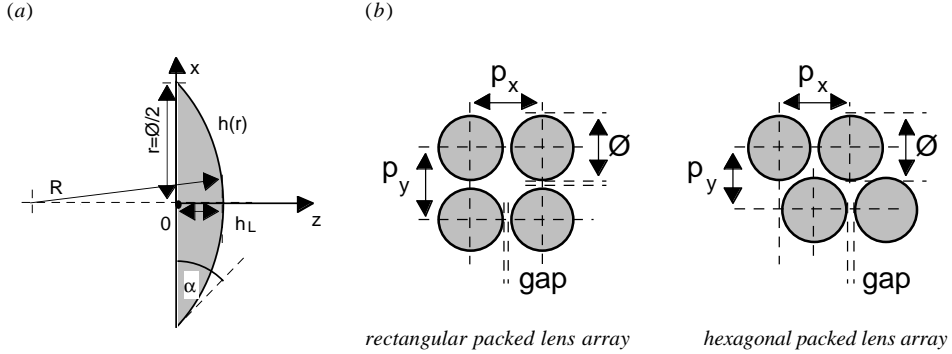


Figure 1. (a) A plano-convex microlens is described by the lens diameter $\varnothing = r/2$, the radius of curvature R , the height at the vertex h_L and the contact angle α at the lens border. (b) Microlens array arrangements. p_x and p_y represent the pitch of the lenses in the x - and y -directions.

$h(r)$ might be spherical ($K = 0$), elliptic ($-1 < K < 0$ or $K > 0$), parabolic ($K = -1$), hyperbolic ($K < -1$) or even more sophisticated. The radius of curvature at the vertex is given by

$$R = (K + 1) \frac{h_L}{2} + \frac{r^2}{2h_L} \quad (2)$$

where h_L is the height at the vertex. The vertex focal length f of a plano-convex refractive lens is given by

$$f = \frac{R}{n(\lambda) - 1} = \frac{h_L + r^2/h_L}{2(n(\lambda) - 1)} \quad (3)$$

where n is the refractive index and λ the wavelength. The focal length f is a function of the wavelength λ due to material dispersion. The contact angle α at the border of a spherical plano-convex lens ($K = 0$) is given by

$$\sin \alpha = \frac{r}{R} = \frac{r}{f(n - 1)}. \quad (4)$$

The Seidel coefficient for spherical aberration of a thin spherical lens ($K = 0$) is given by

$$S_I = (\text{NA})^4 f \frac{n^2}{(n - 1)^2} \quad (5)$$

where NA is the numerical aperture [1]. A plano-convex hyperboloid ($K = -n^2$) has no spherical aberration for a plane wave (perpendicular incidence, planar side versus incident rays) [2]. The F -number of a lens (lens diameter $\varnothing = 2r$) is given by

$$F = \frac{f}{\varnothing} \approx \frac{1}{2\text{NA}}. \quad (6)$$

The diffraction-limited resolution δx and the depth of focus δz are given by

$$\delta x \approx \lambda F \approx \frac{\lambda}{2\text{NA}} \quad (7)$$

and

$$\delta z \approx 4\lambda F^2 \approx \frac{\lambda}{\text{NA}^2}. \quad (8)$$

Both δx and δz are independent of the lens scale. A downscaling of all length parameters does not affect the diffraction-limited resolution of a lens. However, a scaling changes the magnitude of wavefront aberrations which are expressed in fractions of the wavelength. Small lenses have smaller aberrations than large lenses (for the same F -number and wavelength) [3].

2.2. Packing density

Figure 1(b) shows schemes of a rectangular (left) and a hexagonal (right) packed array of circular microlenses. The fill factor η for both arrays is given by

$$\eta = \frac{r^2 \pi}{p_x p_y} \quad (9)$$

where p_x and p_y are the lens pitch and r is the radius. The gap between the lenses is given by $\emptyset - p_x$. Table 1 shows the fill factor η for different arrays. The maximum fill factor is 78.5% ($\pi/4$) for rectangular and 90.6% ($\pi/2\sqrt{3}$) for hexagonal closely packed arrays of circular lenses.

Table 1. Fill factor η for rectangular and hexagonal packed arrays as shown in figure 1(b). \emptyset is the lens diameter and $p_{x,y}$ the pitch of the lenses in the x - and y -directions.

Relation of lens diameter \emptyset and lens pitch p_x	Fill factor η (%)	
	Rectangular $p_x = p_y$	Hexagonal $p_y = \frac{1}{2}\sqrt{3}p_x$
$\emptyset = p_x$	78.5	90.7
$\emptyset = 0.99p_x$	77.0	88.9
$\emptyset = 0.98p_x$	75.4	87.1
$\emptyset = 0.97p_x$	73.9	85.3
$\emptyset = 0.95p_x$	70.9	81.9
$\emptyset = 0.9p_x$	63.6	73.5

3. Fabrication of refractive microlens arrays

Many suitable manufacturing techniques for refractive microlens arrays have been developed [4]. A very promising technique is the reflow or resist-melting technique [5–7]. It uses solely standard semiconductor equipment and processes (resist coating, photolithography, wet processing, etching, etc) and allows the fabrication of large microlens arrays of excellent optical quality for wavelengths from the deep ultraviolet to the far infrared.

3.1. Reflow or resist-melting method

A thin base layer (0.5–1 μm thickness) of positive photoresist is spin-coated on a glass plate. A polymerization bake is used to harden the resist. A second layer (typically 1–100 μm thickness) of positive photoresist is coated on top of the base layer using a SUSS RC 8 spin coater (Suss KG Munich, Germany). A uniformity on the order of $\pm 2\%$ is achieved for thick resist layers. After a prebake at 80–90 $^\circ\text{C}$ (typically 1 h), a chromium-on-glass mask is contact copied in a mask aligner as shown in figure 2. The exposed resist is resolved

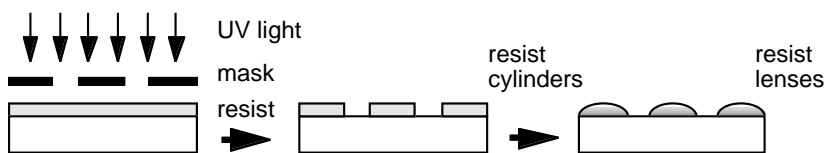


Figure 2. Fabrication of refractive microlenses by the reflow or resist-melting method. (a) Photolithography; (b) developing and (c) melting of the resist structure.

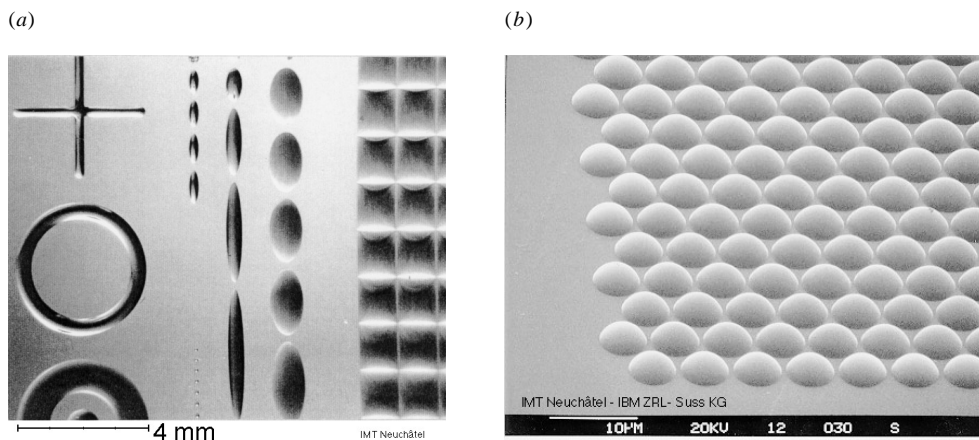


Figure 3. Microlens arrays fabricated by the reflow method. (a) Elliptical, rectangular and ring lenses and (b) an SEM picture of very small microlenses ($\text{\O} \approx 5 \mu\text{m}$, hexagonal densely packed).

in a standard developing process. An array of photoresist cylinders is obtained. The resist cylinders are melted at a temperature of 150–200 °C on a hot plate or in an oven.

The melting procedure itself is quite simple to perform. A melted-resist structure will always act like a microlens. Nevertheless, it is not trivial to fabricate microlenses with good optical performance. The difference between a suitable lens profile and an unacceptable profile is only a fraction of a wavelength. Thus, careful optimization of all processing steps is necessary.

During the melting procedure the edges of the resist structure start melting above the softening temperature [8]. Above the glass transition temperature the amorphous resist polymer changes abruptly from a rubbery state into a glass state system [9]. The surface tension tries to minimize the surface area by rearranging the liquid masses inside the drop [10]. In the ideal case the resist melts completely, the masses are freely transported and surface tension forms a spherical microlens. In practice, a complete melting of the resist drop is not always achievable, especially not in the case of large and flat resist cylinders. For large resist volumes, the outer part of the liquid drop might already be crosslinked (due to out-gassing of the solvents), before the inner part is completely melted. For different lens diameters, height and array types (different packing densities, array size, substrate material) all process parameters such as exposure energy, developing, prebake, cooling, storing conditions, melting cycle, etc have to be carefully optimized. Figure 3 shows different types of microlens arrays fabricated by reflow as described above.

3.2. Fabrication limits for diameter, numerical aperture and packing density

The minimum lens diameter is limited by standard photolithography to 1–2 μm . The upper limit of the lens diameter is determined by the height h_C of the resist structure and the contact angle α at the rim of the lens. The volume of the resist cylinder is given by $V_C = \pi h_C r^2$. The volume of the melted-resist lens V_L is given by

$$V_L = \frac{1}{3}\pi h_L^2(3R - h_L) = \frac{1}{6}\pi h_L(3r^2 + h_L^2) \quad (10)$$

where R is the radius of curvature and h_L is the height at the vertex. Usually, the resist volume shrinks during the heating due to solvent out-gassing and crosslinking ($V_L \leq V_C$). The height of the resist cylinder h_C and the lens h_L are given by

$$h_C \leq \frac{h_L}{2} + \frac{h_L^3}{6r^2} \quad h_L = \gamma h_C \quad \gamma \approx 1.3\text{--}1.7. \quad (11)$$

Usually, the lens is 1.3–1.7 times higher than the resist cylinder before melting. For a spherical lens profile as shown in figure 1(a), the contact angle α is given by

$$\sin \alpha = \frac{r}{R} = \frac{2rh_L}{h_L^2 + r^2} \approx \frac{\text{NA}}{n - 1} \quad (12)$$

or

$$\sin \alpha = \frac{h_L}{\emptyset} \left[\left(\frac{h_L}{\emptyset} \right)^2 + \frac{1}{4} \right]^{-1}. \quad (13)$$

The contact angle α depends on the surface energy, the resist volume and the diameter of the lens base during the melting step. A minimum contact angle of the order of 10° is achieved for melting photoresist on a resist base layer. This minimum contact angle corresponds to a ratio of $h_L/\emptyset \approx 1/23$ for lens height to diameter. Below this ratio the lens profile is deformed in the middle. Reflow microlenses of $h_L/\emptyset > 1/2$ have already been fabricated [4]. The rapidly increasing spherical aberrations (equation (5)) are a severe restriction for plano-convex lenses of high numerical aperture. The total internal reflection of the refracted light at the lens boundaries is another severe limitation for high numerical aperture lenses.

The packing density of lens arrays is given in table 1. A proper separation of the resist cylinders (gap $> 1 \mu\text{m}$) is required for the reflow step. The aspect ratio gap/ h_C for photoresist structures is usually limited to $\frac{1}{5}$ to $\frac{1}{10}$. The minimum lens gap therefore increases with the lens height.

3.3. Transfer in fused silica by reactive ion etching (RIE)

Figure 4 shows the spectral transmission of an 11 μm thick layer of melted photoresist. For applications in the blue and UV wavelength regions the resist lenses are usually transferred in fused silica by reactive ion etching (RIE) [11–14]. RIE transfer in silicon or GaAs is applied for microlenses used in the IR wavelength region [15, 16].

Figure 5 shows the RIE transfer process of resist microlenses in fused silica. Melted-resist lenses are fabricated on a fused silica wafer. The resist shape is transferred in fused silica by RIE. Atoms from the resist surface and the silica are removed simultaneously by energetic ions until the lens shape is completely etched into the substrate. The etch rate of the photoresist and the silica depends strongly on the RIE parameters.

The profile of the microlens might be slightly deformed after the RIE transfer. Usually the lenses are steeper at the rim and flatter at the vertex. Spherical aberrations are severely enhanced due to the profile change and the lower refractive index of the fused silica. A profile modification is done by changing the etch rate during the RIE step. The resist is

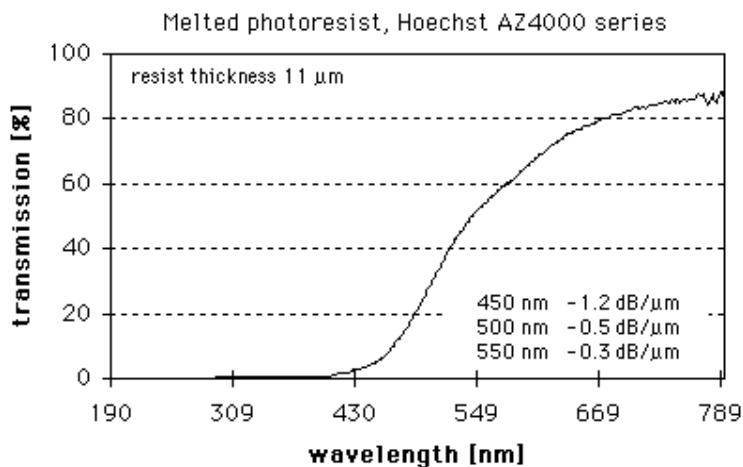


Figure 4. Spectral transmission of an 11 μm thick layer of melted photoresist.

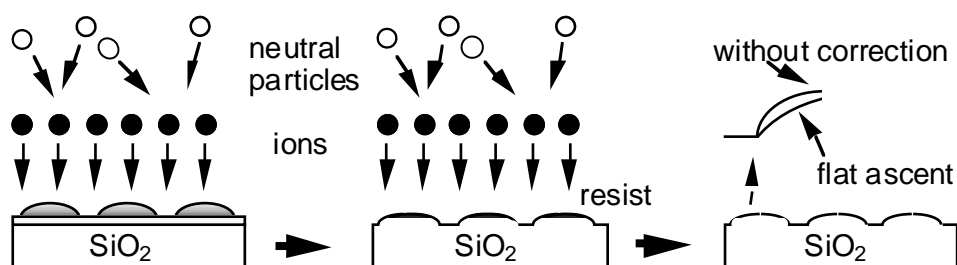


Figure 5. Scheme of the RIE transfer process of resist microlenses in fused silica. A correction of the lens slope is obtained by changing the etch rate between the resist and fused silica during the etching process.

etched more quickly at the beginning and more slowly at the end. The roughness of the lens surface might be significantly increased during the RIE transfer. An adequate wafer cooling is mandatory to avoid puncture of the resist surface during the ion bombardment.

4. Testing of microlenses

A good knowledge of the actual profile is required for the optimization of the fabrication procedure. Various optical and mechanical methods are available to characterize physical and optical properties such as surface profile, surface roughness, wave aberrations, uniformity of the focal length, transmission, refractive index, etc. In the following, we present some test methods used for the optimization of the microlens fabrication steps.

4.1. Mechanical profilometer and AFM

A mechanical stylus profilometer (Tencor alpha step) was used to determine lens height and surface profile. Figure 6(a) shows the profile of a microlens ($\varnothing = 190 \mu\text{m}$, $h = 20 \mu\text{m}$) etched in fused silica versus a spherical profile. The microlens profile is too flat at the centre and too steep at the rim. The asymmetry in the profile is caused by imperfections of

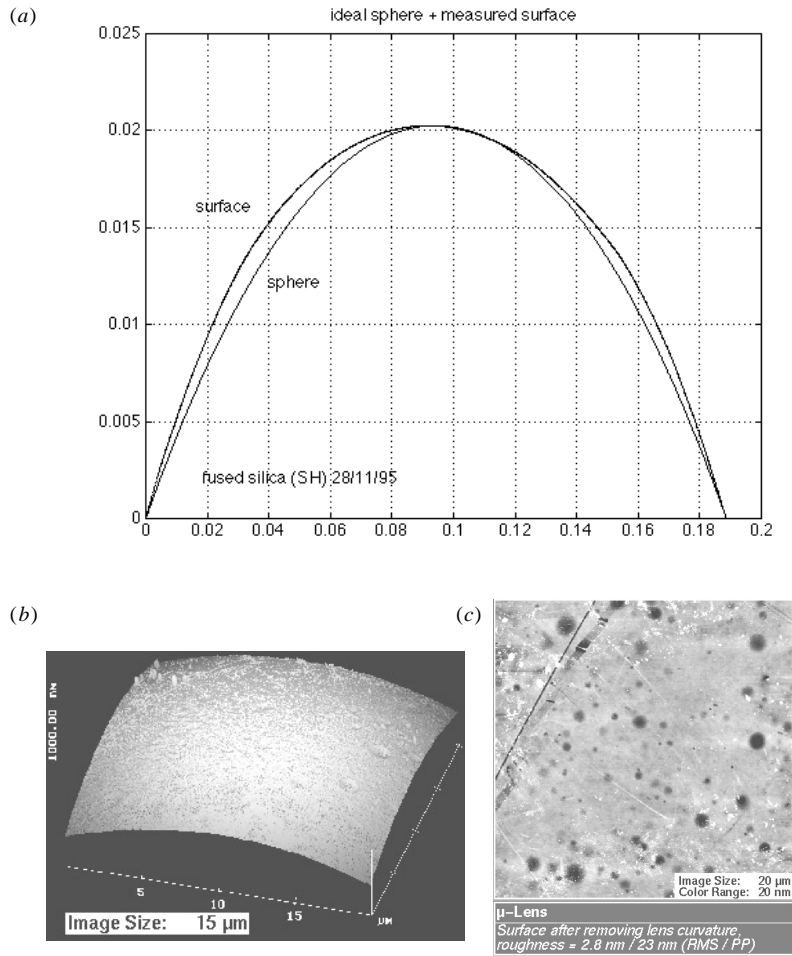


Figure 6. A microlens etched in fused silica: (a) surface profile obtained from a mechanical profilometer, (b) and (c) surface roughness of a small part of a microlens measured using an AFM [17].

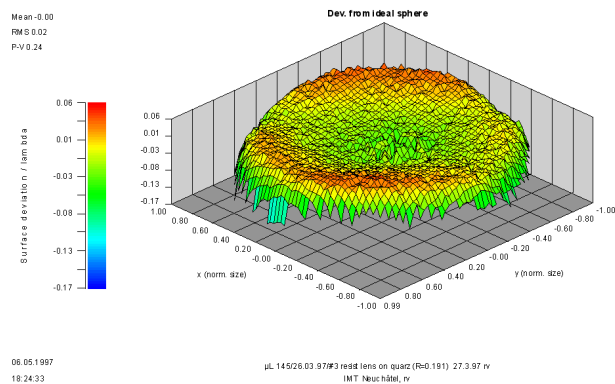
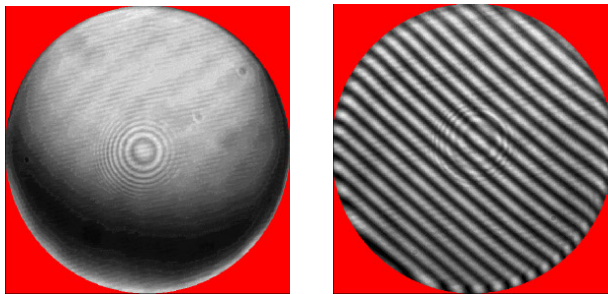
the stylus measurement. A stylus profilometer measures a height difference very precisely, but is only of very limited use in characterizing a continuous lens profile.

Figure 6(b) and (c) show the surface in the centre of a fused silica microlens ($\varnothing = 145 \mu\text{m}$, $h_L = 11 \mu\text{m}$) as measured by an atomic force microscope (AFM) [17]. Due to the limited scanning area a measurement of the lens shape is not practical for large lenses. However, an AFM is very useful for the measurement of the surface roughness. The total integrated scattering (TIS) of an optical surface can be estimated from the RMS surface roughness δ given by

$$\text{TIS} \approx \left(\frac{4\pi\delta}{\lambda} \right)^2. \quad (14)$$

A roughness of 5 nm corresponds to a TIS of 1–2% for visible light. A surface roughness of $\delta < 3 \text{ nm}$ (RMS) corresponding to $\text{TIS} < 1\%$ was found for microlenses etched in fused silica.

(a) microlens: $\varnothing = 0.145 \text{ mm}$, $h_L = 13 \mu\text{m}$



(b) microlens: $\varnothing = 1 \text{ mm}$, $h_L = 70 \mu\text{m}$

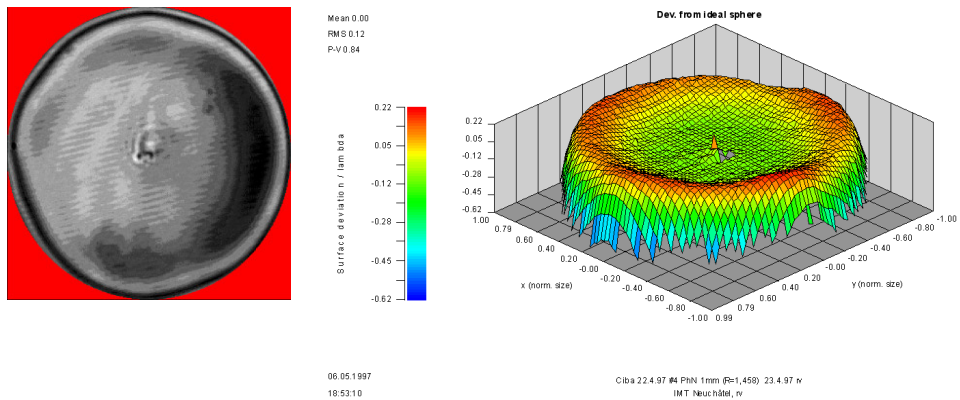


Figure 7. Interferograms and the deviation from a perfect sphere for resist microlenses of $145 \mu\text{m}$ and 1 mm lens diameter measured in a Twyman–Green interferometer.

4.2. Interferometric microlens testing

4.2.1. Twyman–Green interferometer. A Twyman–Green interferometer (Mikos Erlangen, Germany) providing a variable magnification (lens diameters from $50 \mu\text{m}$ to 2 mm) and

phase-shift software was used to test the surfaces of microlenses [18, 19]. The Twyman–Green interferometer measures the deviation of the surface profile from an ideal sphere. In addition, the interferometer allows measurement of the radius of curvature R at the vertex with an accuracy of better than 1%. Figure 7(a) shows interferograms (zero fringes, tilted fringes) and the deviation from a perfect sphere for a resist microlens of $145\ \mu\text{m}$ diameter, $13\ \mu\text{m}$ height and a vertex radius of curvature of $191\ \mu\text{m}$ measured in a Twyman–Green interferometer. A deviation from a perfect sphere of $< \lambda/20$ (RMS) and $\lambda/4$ (p/v) was observed. Figure 7(b) shows an interferogram (zero fringes) and the deviation from a perfect sphere for a resist microlens of $1\ \text{mm}$ diameter, $70\ \mu\text{m}$ height and a vertex radius of curvature of $1.46\ \mu\text{m}$. A deviation from a perfect sphere of $\lambda/8$ (RMS) and 0.84λ (p/v) was observed.

Figure 8(a) shows the interferogram of a lens ($\varnothing = 145\ \mu\text{m}$) before and (b) after RIE transfer into fused silica inspected in a Twyman–Green interferometer. A deviation from a perfect sphere of $\lambda/10$ (RMS) has been achieved for the microlens in fused silica.

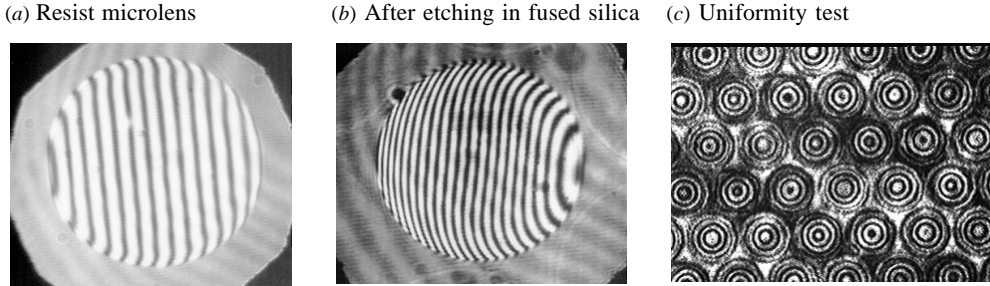


Figure 8. Interferogram of a microlens ($\varnothing = 145\ \mu\text{m}$) (a) before and (b) after RIE transfer, tested in a Twyman–Green interferometer and (c) interferogram of a uniformity test in a Michelson interferometer.

4.2.2. Michelson interferometer. The uniformity of a lens array depends mainly on the accuracy of the resist cylinders and the melting procedure. A Michelson interferometer was used to test the uniformity of a lens array ($\varnothing = 190\ \mu\text{m}$, $f = 500\ \mu\text{m}$). One mirror of the interferometer was set in the focal plane of the lenses. Figure 8(c) shows an interferogram. The measured uniformity of the focal length was better than 1%.

4.2.3. Mach–Zehnder interferometer. A Mach–Zehnder interferometer was used to measure the wave aberrations of plano-convex refractive microlenses [20].

Figure 9(a) shows an interferogram of a resist lens ($\varnothing \approx 150\ \mu\text{m}$, $\text{NA} \approx 0.15$) tested in a Mach–Zehnder interferometer. Figure 9(b) shows the modulation transfer function (MTF) calculated from the wave aberrations. Diffraction-limited performance is observed for the lens shown in figure 9(a).

4.2.4. Correlation of Twyman–Green and Mach–Zehnder measurements. A Twyman–Green interferometer allows a full description of a curved surface. A Mach–Zehnder interferometer measures the wave aberrations directly. Both results can be crosschecked by using ray-tracing analysis [21]. A plano-convex microlens in fused silica ($\varnothing = 145\ \mu\text{m}$, $h_L = 11.3\ \mu\text{m}$) was measured using a Twyman–Green and a Mach–Zehnder

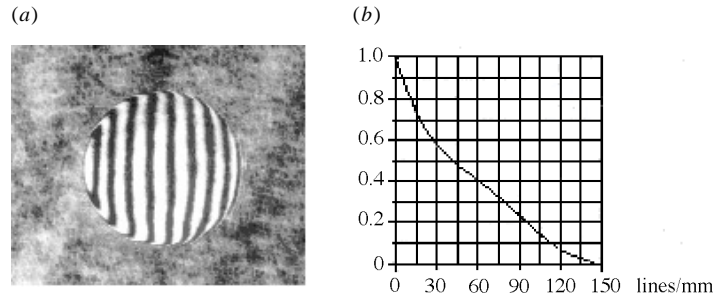


Figure 9. The wave aberrations of a resist microlens ($\varnothing \approx 150 \mu\text{m}$, $\text{NA} \approx 0.15$) were tested in a Mach–Zehnder interferometer. (a) Interferogram and (b) the MTF calculated from the wave aberrations.

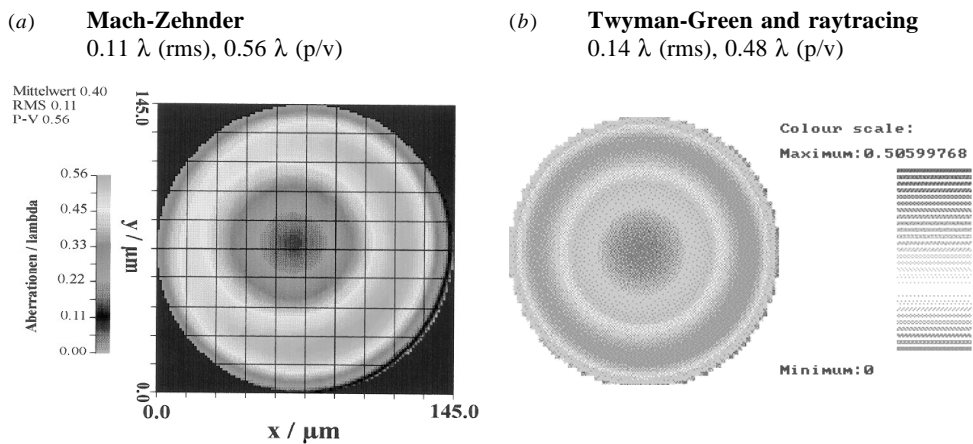


Figure 10. Greyscale plot of the wave aberrations for a refractive microlens ($\varnothing = 145 \mu\text{m}$, $h_L = 11.3 \mu\text{m}$) in fused silica. (a) Directly measured aberrations in a Mach–Zehnder interferometer. (b) Aberrations calculated by ray-tracing analysis from the surface measurement in a Twyman–Green interferometer.

interferometer. The wave aberrations of the measured surface were calculated by ray-tracing analysis. Figure 10 shows greyscale plots of (a) the directly measured aberrations in a Mach–Zehnder interferometer and (b) the aberrations calculated by ray-tracing analysis from the surface measurement in a Twyman–Green interferometer. The results from the different measurements show a good correlation. A precondition for this crosscheck of reflection and transmission interferometry is a constant refractive index within the lens volume. In the case of microlenses etched in fused silica, the fluctuations of the index are certainly negligible. This might not be the case for microlenses in photoresist.

4.3. Inspection of the focal plane

A very simple test method is the visual inspection of the focal plane in a microscope. A pinhole, micro-objective or fibre is placed in the illumination part of a microscope. The point source is imaged by the microlenses placed on the microscope stage. Spot (or line) images observed in the microscope are shown in figure 11. Similar set-ups are used for

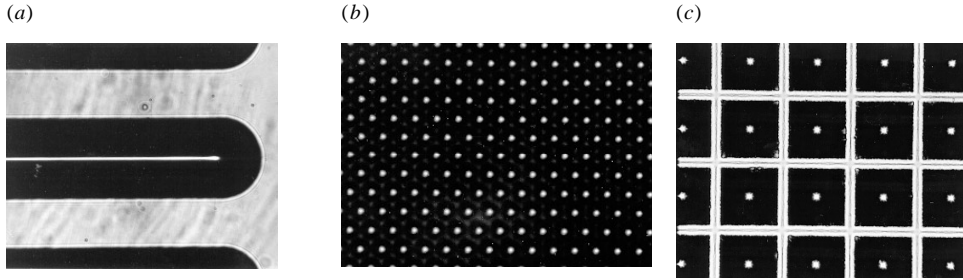


Figure 11. Visual inspection of the focal plane in a microscope with white light illumination. (a) Focal plane of cylindrical microlenses (0.6 mm lens width), (b) a microlens array (5 μm lens diameter) as shown in figure 3(b) and (c) square lenses (400 μm lens width).

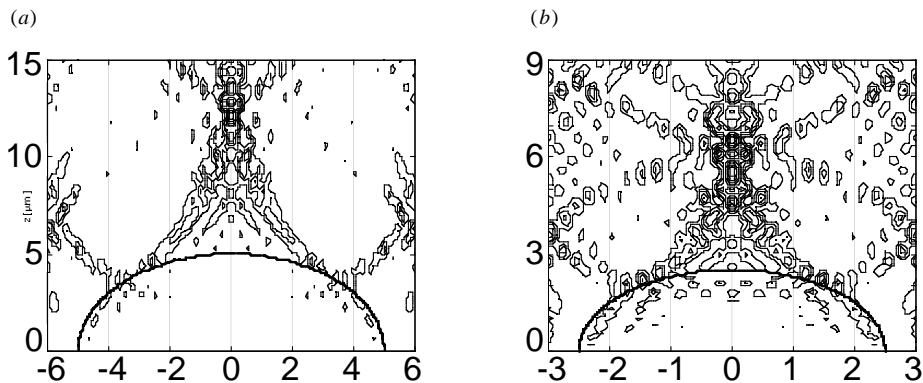


Figure 12. Distribution of the light intensity behind a microlens of 5 μm diameter and 2.5 μm height, calculated by rigorous diffraction theory. A depth of focus of $\delta z > 5 \mu\text{m}$ is found for a spot diameter of $\delta x \leq 1 \mu\text{m}$.

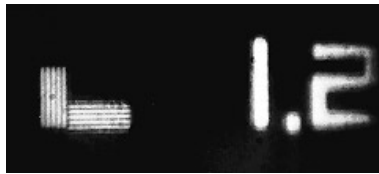


Figure 13. Test pattern imaged using a single resist microlens ($\text{Ø} = 250 \mu\text{m}$, $\text{NA} = 0.36$). A resolution of 400 lines/mm (1.2 μm feature size) is observed in a microscope under white light illumination.

direct measurements of the point spread function (PSF) and the modulation transfer function (MTF) [22, 23].

4.4. Very small microlenses

Very small microlenses with diameters of a few microns are fabricated occasionally [24]. Lenses which are in the range of the wavelengths of light cannot be evaluated by ray-tracing or conventional diffraction theory. A more rigorous analysis is necessary. Figure 12 shows the distribution of the light intensity behind a plano-convex cylindrical microlens of (a)

$10\ \mu\text{m}$ width and $5\ \mu\text{m}$ height and (b) $5\ \mu\text{m}$ width and $2.5\ \mu\text{m}$ height, both calculated by rigorous diffraction theory (for TE polarization) [25].

In figure 12(b) the distribution of the light is significantly different from that obtained by ray-tracing. The light is ‘funnelled’ in a small pipe of $\delta x \leq 1\ \mu\text{m}$ diameter and $\delta z > 5\ \mu\text{m}$ length.

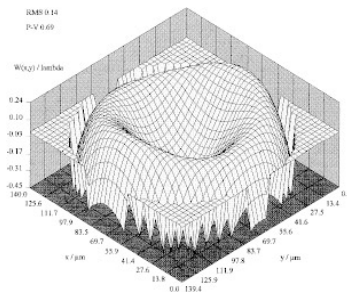
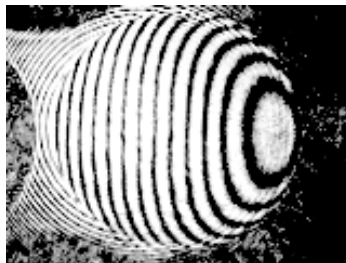
4.5. Resolution test

The image resolution of a microlens was tested in a microscope using a test target. Melted-resist microlenses are well suited for high-resolution imaging. Figure 13 shows the image of a test pattern imaged using a melted-resist lens ($\text{Ø} = 250\ \mu\text{m}$, $\text{NA} = 0.36$). A resolution of $1.2\ \mu\text{m}$ (≈ 400 lines/mm) is observed in a microscope with white light illumination.

5. Replication

Resist microlens arrays may serve as master elements for replication. Figure 14 shows the wave aberrations of a resist master ($\text{Ø} = 140\ \mu\text{m}$, $h = 13.2\ \mu\text{m}$) replicated by casting in a PMMA-type organic glass [26]. The wave aberrations of the microlenses were measured in a Mach–Zehnder interferometer [20]. Wave aberrations of 0.14λ (RMS) were found for both master and replica. No significant difference between the master and the replicated lens arrays could be observed.

(a) Resist master



(b) Replica

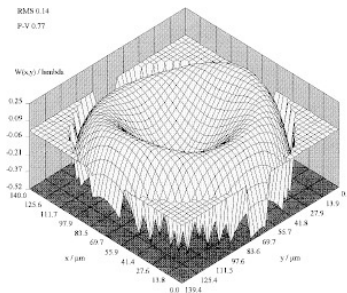
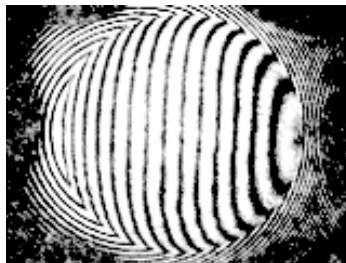


Figure 14. Replication of a resist lens in organic glass. The wave aberrations of (a) the lens master (RMS 0.14λ , $p/v\ 0.69\lambda$) and (b) the replica (RMS 0.14λ , $p/v\ 0.77\lambda$) were measured in a Mach–Zehnder interferometer.

6. Packaging and alignment

Microsystem technology combines a variety of opto-electronic, mechanical and micro-optical elements or modules. A typical optical microsystem consists of light sources,

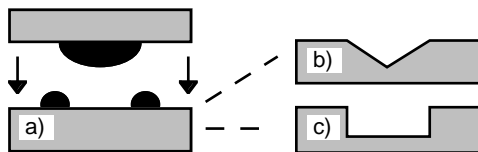


Figure 15. Self-alignment of a microlens versus (a) a ring lens, (b) a V-groove or (c) a hole or slit.

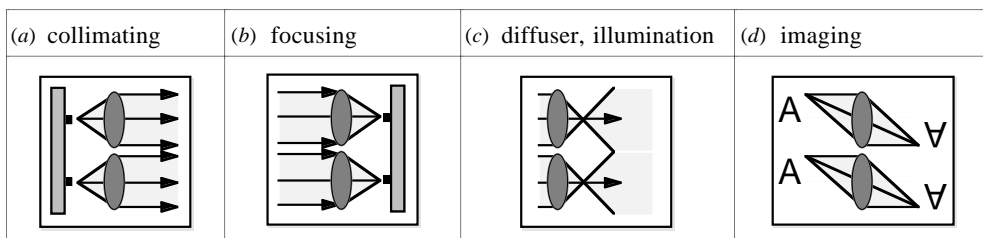


Figure 16. Basic optical functionality carried out by microlens arrays.

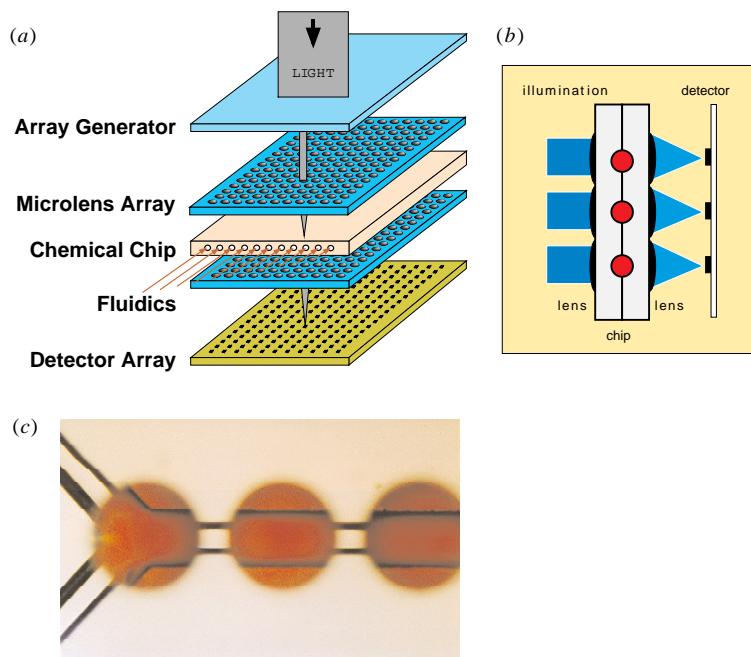


Figure 17. (a) and (b) Scheme of a μ TAS using microlens arrays for illumination and detection in parallel microcapillaries of a chemical chip and (c) spherical microlens ($\varnothing = 600 \mu\text{m}$) on top of a capillary ($100 \mu\text{m}$ width).

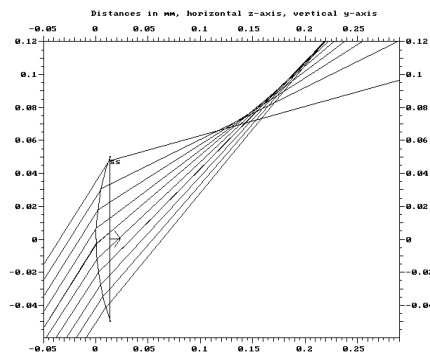
detectors, active and passive optical components. For multiple-channel processing or detection these elements are often arranged side-by-side on planar substrates. Different layers or modules have to be aligned with each other in six degrees of freedom. Standard semiconductor methods such as anodic and flip-chip bonding in a bond aligner are widely used but rather time consuming [27]. A very simple self-alignment method for two planar layers is shown in figure 15.

A spherical plano-convex microlens aligns itself in (a) a ring lens (as shown in figure 3(a)), a V-groove, (c) a hole or groove or any other corresponding structure. The alignment lenses are fabricated using the standard reflow process.

7. Applications

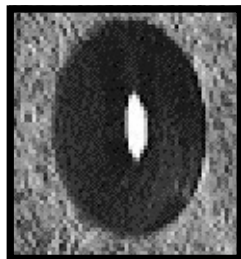
Microlens arrays are used for collimating or focusing (laser arrays, detector arrays, fibre optics, sensors, optical interconnects, optical computing, etc), for illumination (flat panel displays, TV projection systems, retro-reflectors, diffusers, etc) and for imaging

(a) Raytracing



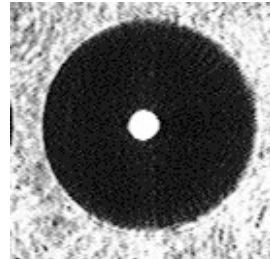
$$(\alpha = 45^\circ, f = 1.92 \text{ mm})$$

(b) Meridional focal plane of (a)



$$(\alpha = 45^\circ)$$

(c) Focal plane of elliptical lens



$$(\alpha = 48^\circ)$$

Figure 18. (a) Ray-tracing analysis for a spherical microlens ($\varnothing = 1 \text{ mm}$) illuminated under an angle of $\alpha = 45^\circ$. (b) Meridional focal plane of the spherical lens. (c) The focal plane of an elliptical lens ($1.5 \text{ mm} \times 1 \text{ mm}$) for $\alpha = 48^\circ$.

(photocopiers, 3D-photography, signal and image processing, fibre couplers, microlens lithography, shop testing, astronomy, etc). Typical tasks for microlens arrays are shown in figure 16. In the following, we will present examples for the system integration of refractive microlenses.

7.1. Chemical microchips and μ TAS

Chemical microchips and miniaturized total analytical systems (μ TAS) cover a wide range of disciplines, such as analytical and organic chemistry, biochemistry, electronics, microengineering, solid state physics, laser physics and micro-optics. Usually, a complex arrangement of lasers, detectors, filters, optics and high-precision mechanical stages is required for illumination and optical detection. Microlens arrays offer a large potential to reduce the size and to simplify the architecture of analytical systems. Figures 17(a) and (b) show schemes of a μ TAS using microlens arrays for parallel illumination and detection of microcapillaries and (c) spherical microlens ($\varnothing = 600 \mu\text{m}$) on top of a capillary ($100 \mu\text{m}$ width) [28].

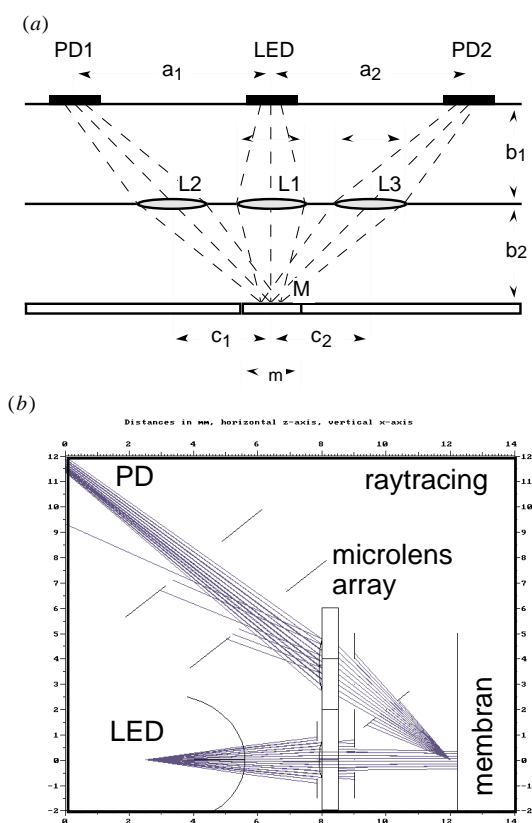


Figure 19. Optical blood gas sensor using elliptical microlenses (L2, L3) for detection. (a) Scheme of the optical set-up. (b) Ray-tracing analysis for the illumination and detection system.

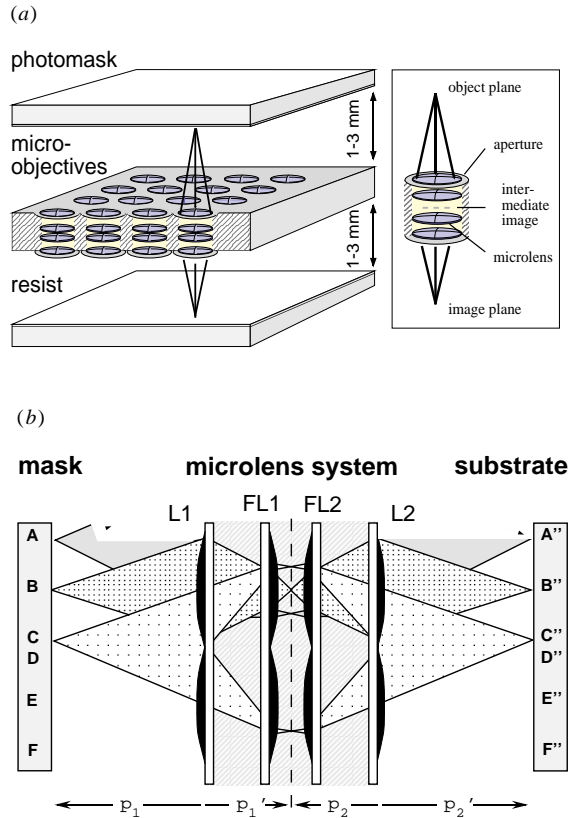


Figure 20. (a) An array of micro-objectives images a mask onto a resist layer. The diameter of the micro-objective channel is typically 0.1–0.5 mm. (b) Scheme of two adjacent micro-objective channels. Lens arrays L1 and L2 are used for imaging. Lens arrays FL1 and FL2 serve as a field lens.

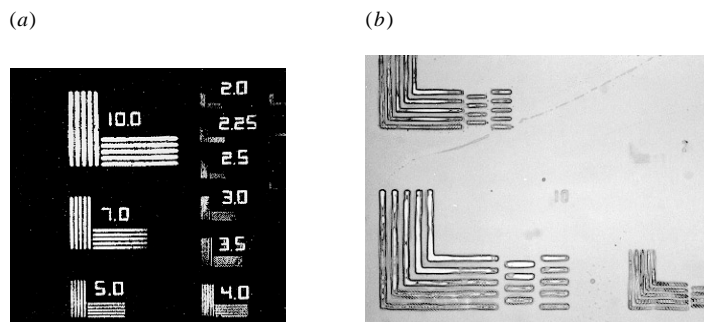


Figure 21. (a) Image plane observed in a microscope with white light illumination. (b) Test pattern (5, 7, 10 μm feature sizes) printed with microlens lithography in photoresist (in SUSS MA 150 mask aligner (g, h and i line)).

7.2. Off-axis microlenses for optical blood gas sensor

Elliptical microlenses [29] were used to compensate the astigmatism for off-axis imaging, e.g. for chemical sensor heads. Figure 18(a) shows a ray-tracing analysis for a light beam

of $\alpha = 45^\circ$ incidence focused by a spherical microlens ($\varnothing = 1 \text{ mm}$) and (b) shows the meridional focal plane. The astigmatism is corrected for a given angle α by using an elliptical lens base. The geometry of the lens base is given by $\cos(\alpha) \approx y/x$. Figure 18(c) shows the focal plane of an elliptical lens ($1.5 \text{ mm} \times 1 \text{ mm}$) for light incident at an angle of $\alpha = 48^\circ$. Elliptical microlenses have been used in an optical blood gas sensor as shown in figure 19 [30]. The light from a LED is collimated by lens L1 and illuminates a membrane. The fluorescent light is imaged onto the photodiodes PD by elliptical microlenses (L2, L3).

7.3. Microlens array imaging system for photolithography

A microlens array imaging system was developed in connection with a new contactless photolithographic technique called microlens lithography [31–33]. This new lithographic imaging technique provides an increased depth of focus ($>50 \text{ }\mu\text{m}$) at a larger working distance ($>1 \text{ mm}$) than is customary with proximity printing. Potential applications are photolithography for large print areas (flat panel displays, colour filters), for thick photoresist layers (micro-mechanics), printing on curved surfaces (or substrates with a poor planarity) or in V-grooves. Figures 20(a) and (b) show the optical set-up. An array of micro-objectives is used to project a photomask onto a resist layer ($\beta = +1$ imaging).

A micro-objective array is formed by a stack of microlens and aperture arrays. Each objective transports a part of the mask pattern. The individual images overlap coincidentally to generate a single, complete image of the mask [34]. Micro-objective imaging systems were assembled and integrated into a mask aligner to perform test prints in photoresist. Figure 21(a) shows the image plane observed in a microscope and (b) a resist pattern printed by microlens lithography. A theoretical resolution of $3 \text{ }\mu\text{m}$ was calculated by ray-tracing for the whole image field [33].

7.4. Smart mask lithography

Smart mask lithography [35] is aimed at the printing of simple patterns, such as a matrix of micro-dots, posts or holes, or other patterns consisting of lines, dots, circles or squares. A smart mask consists of one (or more) layer(s) of micro-optical elements, such as refractive or diffractive microlenses (spherical, cylindrical or elliptical shape), gratings, CGH, apertures, etc.

A conventional photomask blocks a major part of the illuminating light by a chromium-on-glass layer as shown in figure 22. The pattern is printed by shadowing (contact and

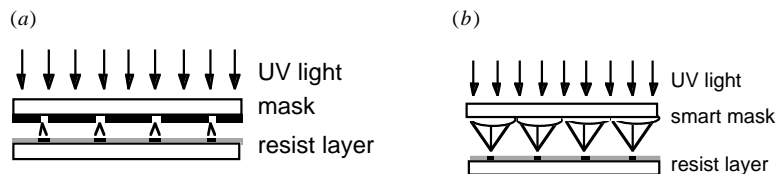


Figure 22. (a) Conventional mask for contact or proximity printing of a dot matrix. The majority of the light is blocked by a chromium layer. The mask is located close to the resist layer. (b) Smart mask for printing a dot matrix. The mask consists of an array of spherical microlenses (typically $5\text{--}50 \text{ }\mu\text{m}$ lens diameter).

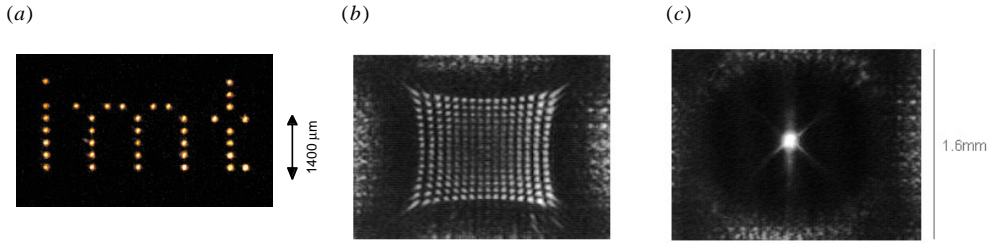


Figure 23. (a) Laser array collimated by using a microlens array, (b) partial demagnification of a 16×16 pixel array ($30 \mu\text{m}$ pixel size, $0.9 \text{ mm} \times 0.8 \text{ mm}$ array size) and (c) integration of all pixels in one spot of $200 \mu\text{m}$ diameter.

proximity printing), or imaging (wafer stepper and projection systems). A smart mask generates the desired pattern in a photosensitive resist layer. The resist layer is in contact ($0\text{--}5 \mu\text{m}$), at a short distance ($5\text{--}100 \mu\text{m}$), or far behind the mask ($>100 \mu\text{m}$). The mask pattern and the printed pattern are not identical. Figure 22(a) shows a conventional photomask and (b) a smart mask. Here, the smart mask consists of an array of plano-convex spherical microlenses to print a dot matrix.

Each lens concentrates the incoming light to a focus. The resist layer is located in the focal plane. The light is ‘funnelled’ in a small pipe of $\delta x \leq 1 \mu\text{m}$ diameter and $\delta z > 5 \mu\text{m}$ length as shown in figure 12. Flexible or conformable smart masks can be used (in soft or vacuum contact) to compensate the waviness or other minor surface defects of the resist layer.

7.5. Microlens arrays for optical signal processing

Microlens arrays are widely used in optical computing and neural networks. Typical tasks are in the collimating of light sources, e.g. a surface emitting laser array as shown in figure 23(a) [36]. Microlens arrays could be used as fan-in elements as shown in figures 23(b) and (c). A pixel matrix from a laser array or LCTV is demagnified using a large microlens ($\text{Ø} = 1.4 \text{ mm}$). The demagnified images of the single pixels overlap in one spot with a diameter of $\text{Ø}_{\text{spot}} \approx 200 \mu\text{m}$ [37].

Acknowledgments

Our work was partially supported by the Swiss Priority Programs OPTIQUE and MINAST, Hugel Lithography (Brissago, Switzerland), Karl Suss (Munich, Germany) and Novartis (Basel, Switzerland). The authors thank I Philipoussis, J Ch Roulet, Ch Berger, A Pourzand, P Blattner, S Verpoorte, K Fluri (IMT Neuchâtel, Switzerland), N Lindlein, B Manzke, H Schreiber, J Schwider (University Erlangen, Germany), A E Bruno, D Anselmetti (Novartis Basel, Switzerland), E Cullmann, S Seider (Karl Suss Munich, Germany) and E Noordhanus (Philips Eindhoven, Netherlands).

References

- [1] Herzig H P (ed) 1997 *Micro-optics* (London: Taylor and Francis)
- [2] Naumann H and Schroeder G 1992 *Bauelemente der Optik* (Munich: Hanser)
- [3] Lohmann A W 1989 Scaling laws for lens systems *Appl. Opt.* **28** 4996–8
- [4] 1991 *Conf. on Microlens Arrays, IOP Short Meeting Series* (Teddington: NPL)
- 1993 *Conf. on Microlens Arrays, EOS Topical Meeting Digest Series* vol 2
- 1995 *Conf. on Microlens Arrays, EOS Topical Meeting Digest Series* vol 5
- 1997 *Conf. on Microlens Arrays, EOS Topical Meeting Digest Series* vol 13
- [5] Popovic Z D, Sprague R A and Neville-Connell G A 1988 Technique for monolithic fabrication of microlens arrays *Appl. Opt.* **27** 1281
- [6] Daly D, Stevens R F, Hutley M C and Davies N 1990 The manufacture of microlenses by melting photoresist *J. Meas. Sci. Technol.* **1** 759–66
- [7] Haselbeck S, Schreiber H, Schwider J and Streibl N 1993 Microlenses fabricated by melting photoresist *Opt. Eng.* **6** 1322–4
- [8] Gogolides E, Tegou E, Beltsios K, Papadokostaki K and Hatzakis M 1996 Thermal and mechanical analysis of photoresist and silylated photoresist films: application to AZ 5214 *Microelectron. Eng.* **30** 267–70
- [9] Moreau W M 1988 *Semiconductor Lithography* (New York: Plenum)
- [10] Jay T R, Stern M B and Knowlden R E 1992 Effect of refractive microlens array fabrication parameters on optical quality *SPIE* **1751** 236–45
- [11] Eisner M, Haselbeck S, Schreiber H and Schwider J 1993 Reactive ion etching of microlens arrays into fused silica *EOS Topical Meeting Digest* vol 2, pp 17–9
- [12] Gratix E 1993 Evolution of a microlens surface under etching conditions *SPIE* **1992** 266–74
- [13] Stern M B and Jay T R 1994 Dry etching for coherent refractive microlens arrays *Opt. Eng.* **33** 3547–51
- [14] Mersereau K, Nijander C R, Townsend W P and Feldblum A Y 1996 *Technical Digest of the Topical Meeting on Diffractive Optics and Micro-Optic* (Boston, MA, 1996) (OSA)
- [15] Eisner M and Schwider J 1996 Transferring resist microlenses into silicon by RIE *Opt. Eng.* **35** 2979–82
- [16] Strezlecka E M, Robinson G D, Peters M G, Peters F H and Coldren L A 1995 Monolithic integration of vertical-cavity laser diodes with refractive GaAs microlenses *Electron. Lett.* **31** 724–5
- [17] Anselmetti D Measurement at Novartis Pharma Basel, Switzerland
- [18] Schwider J *Twyman–Green interferometer and PSI software from Mikos* University of Erlangen, Erlangen, Germany
- [19] Schwider J and Falkenstörfer O 1995 Twyman–Green interferometer for testing microspheres *Opt. Eng.* **34** 2972–5
- [20] Schwider J Measurement at University Erlangen, Erlangen, Germany
- [21] Lindlein N *Raytrace 6.1* University of Erlangen, Erlangen, Germany
- [22] Hutley M C, Daly D and Stevens R F 1991 The testing of microlens arrays *IOP Short Meeting Series* vol 30, pp 67–81
- [23] Gao Y and Hutley M C 1995 The chromatic dispersion of microlenses *EOS Topical Meeting Digest* vol 5, pp 65–9
- [24] Ensell G, Evans A, Farooqui M, Haycocks J A and Stedman M 1993 Nanometrological micromachined artefacts *EOS Topical Meeting Digest Series* vol 2, pp 9–12
- [25] Blattner P and Herzig H P 1997 Rigorous diffraction theory applied to microlens arrays *EOS Topical Meeting on Diffractive Optics* (Savonlinna, 1997)
- [26] Philips Components, Eindhoven, The Netherlands
- [27] Lee Y C and Basavanahally N 1994 Solder engineering for optoelectronic packaging *J. Metals* June 45–50
- [28] Project 1.05 MicroTAS 1997 *Proc. on Minast 1st Ann. Convention Swiss Priority Program in Micro and Nano System Technology* (Bern, 1997) pp 44–5
- [29] Mersereau K, Nijander C R, Townsend W P, Crisci R J, Feldblum A Y and Daly D 1991 Design, fabrication, and testing of refractive microlens arrays *IOP Short Meeting Series* vol 30, pp 60–8
- [30] Bruno A E, Barnard St, Ehrat M, Völkel R, Nussbaum Ph and Herzig H P 1996 Optische Detektionsvorrichtung für chemische Analysen an kleinvolumigen Proben *European patent application* no 96810341.6
- [31] Hugle W B, Daendliker R and Herzig H P 1992 Lens array photolithography *GB patent application* 9224080.3
- Hugle W B, Daendliker R and Herzig H P 1993 Lens array photolithography *US patent* 08/114,732
- [32] Dändliker R, Gray S, Clube F, Herzig H P and Völkel R 1995 Non-conventional fabrication methods for photolithography *Microelectron. Eng.* **27** 205–11

- [33] Völkel R, Herzig H P, Nussbaum Ph and Dändliker R 1996 Microlens array imaging system for photolithography *Opt. Eng.* **35** 3323–30
- [34] Anderson R H 1979 Close-up imaging of documents and displays with lens arrays *Appl. Opt.* **18** 477–84
- [35] Völkel R, Herzig H P, Nussbaum Ph, Blattner P, Dändliker R, Cullmann E and Hugle W B 1997 Microlens lithography and smart masks *MNE'96 (Glasgow) Microelectronic Engineering* vol 35, pp 513–6
- [36] Collings N, Pourzand A R and Völkel R 1995 The construction of a programmable multilayer analogue neural network using space invariant interconnects *SPIE* **2565** 40–7
- [37] Berger Ch, Collings N, Pourzand A R and Völkel R 1995 A reconfigurable interconnect for neural network and switching applications *EOS Topical Meeting Digest Series* vol 9, pp 50–1